



# Impedance spectroscopy of nanostructured ZnO morphologies

Rusiri Rathnasekara<sup>1</sup>, Parameswar Hari<sup>1,2,a)</sup>

- <sup>1</sup>Department of Physics and Engineering Physics, University of Tulsa, Tulsa, OK 74104, USA
- <sup>2</sup>Oklahoma Photovoltaic Research Institute, University of Tulsa, Tulsa, OK 74104, USA
- a) Address all correspondence to this author. e-mail: hari@utulsa.edu

Received: 9 January 2021; accepted: 20 April 2021

In this study, four nanostructured ZnO morphologies, nanoribbons, nanorods, nanoparticles, and nanoshuttles, were synthesized at annealing temperatures of 300 °C, 500 °C, and 700 °C. Structural properties were studied by Scanning Electron Microscopy (SEM), Transmission Electron Microscopy (TEM), X-ray Diffraction Spectroscopy (XRD), and Differential Scanning Calorimetry (DSC). Optical properties were analyzed by UV–Visible Spectroscopy and Photoluminescence (PL). Electrical transport properties were studied by the Cole–Cole plot technique and electrical resistivity. From the impedance spectroscopy analysis, we extracted the carrier lifetime, the RC time constant, and grain and grain boundary parameters in each morphology. We observed that resistance decreased with increasing temperature in all samples in general, while nanorods, nanoshuttles, and nanoribbons showed well-defined semicircle profiles due to grain and grain boundaries at higher temperatures. From wettability studies, we obtained that surface with ZnO nanoparticles has hydrophobic properties, while nanorods, nanoribbons, and nanoshuttles resulted in a superhydrophobic surface. The optimum ZnO nanomorphology based on impedance studies can be used for developing electrodes for dye-sensitized solar cells.

#### Introduction

Among the various nanomaterials, Zinc Oxide (ZnO) is one of the most versatile n-type semiconductors. ZnO has a stable wurtzite structure with lattice parameter a=b=0.3250 nm and c=0.5207 nm [1]. Besides, ZnO has special optical, electrical, mechanical, thermodynamic, and electrodynamic properties [2], such as a direct wide bandgap of 3.37 eV giving better transparency at room temperature, a large free exciton binding energy of about 60 meV, high electron mobility, and high thermal conductivity [3, 4]. Furthermore, nanostructured ZnO is an environmentally friendly, highly stable material with low toxicity, and is cost-effective for semiconductor device applications [5].

ZnO has important applications such as biosensors, gas sensors, solar cells, photocatalysis, transistors, and photodiodes [6–11]. Synthesis of different nanostructured morphologies and particle sizes is a critical factor in device and medical applications [12]. ZnO can be synthesized with different morphologies such as nanorods, nanoflowers, nanodiscs, nanobelts,

nanotubes, nano-ellipsoids, and nanoparticles [13–19]. ZnO nanocrystals have been grown using a wide range of techniques such as sol–gel, pulsed laser deposition, hydrothermal, spray pyrolysis, microwave-assisted techniques, precipitation method, chemical bath deposition (CBD), and chemical vapor deposition (CVD) [20–27]. Among these techniques, chemical bath deposition and microwave methods are attractive because they are relatively simple and cost-effective techniques that yield uniform growth.

Several physical and chemical parameters control the synthesis of the ZnO nanoparticle's size and morphology. The pH value of the solution is one of the important parameters in the solution-based synthesis process. The pH value has a significant influence on the properties and morphology of the ZnO nanostructure [28]. From previous studies by Zhang et al., the pH value is known to control the number of ZnO nuclei and growth units [29]. Besides, preparation methods and chemicals play an important role in controlling the morphology of nanostructures. Tamar et al. have reported that different synthesized

solvents also control the stabilization of specific crystallographic planes in growing nanocrystals [30]. For instance, Wenhui et al. have controlled several ZnO morphologies by pretreatment of synthesized solution [31]. Li et al. showed that ZnO particle size specifically depends on the solution conditions [32]. Moreover, annealing temperature also significantly influences the transport properties of nanostructures.

This study aims to compare the structural, optical, electrical, and wetting properties of four different ZnO nanostructures, namely, nanoribbons, nanorods, nanoparticles, and nanoshuttles at three different annealing temperatures, 300 °C, 500 °C, and 700 °C, and to evaluate them for electrodes used in fabricating dye-sensitized solar cells.

#### **Results**

#### Structural analysis

The morphology and particle size of all samples are investigated by scanning electron microscopy (SEM) and transmission electron microscopy (TEM) techniques. Figure 1 shows morphology difference and particle diameter size of ZnO nanostructures, namely, nanoribbons, nanorods, nanoshuttles, and nanoparticles. Image J software was applied to measure the diameter of all ZnO nanostructures. We obtained different morphologies by changing chemical composition and synthesis methods. Yildirim et al. also reported that the size and morphologies can be

controlled by various processing parameters such as reaction temperature and solvent type [33]. From Fig. 1f, we observed an increase in ZnO nanostructure parameters with increasing annealing temperature from 300 °C to 700 °C. ZnO nanoribbons have shown a remarkable enhancement in the diameter of 104 nm to 255 nm with increasing temperature up to 700 °C.

From Fig. 1c, it is clearly shown that the ZnO nanorods have grown perpendicular to the FTO substrate. ZnO nanorods diameter size increased from 68 nm to 219 nm as the annealing temperature increased from 300 to 700 °C. With the rising annealing temperature, the ZnO nanoparticles show an increment in diameter, from 8.48 to 16.99 nm. At 300 °C, the ZnO nanoshuttles have a diameter of around 125 nm, and it increased significantly to 219 nm at 700 °C annealing temperature.

The crystal nature of ZnO nanostructures was studied using the XRD technique. Figure 2 shows the XRD pattern of nanoribbons, nanorods, nanoparticles, and nanoshuttles at 300 °C, 500 °C, and 700 °C annealing temperatures. The XRD peaks at (100), (002), (101), (102), and (110) indicate hexagonal structure of ZnO nanostructures according to JCPSD card no 36-1451 [34]. The other diffraction peaks (002), (101), and (102) also confirmed hexagonal-structured Zinc corresponding to JCPDS card no 04-0831 [35]. The intensity of (100), (002), and (101) peaks of ZnO indicated the behavior of crystallinity nature of nanostructures. It is observed that all samples are highly crystalline, and the intensity of peaks increased sharply for annealing temperature. From Fig. 2b, it has high intensity (002) diffraction peak which

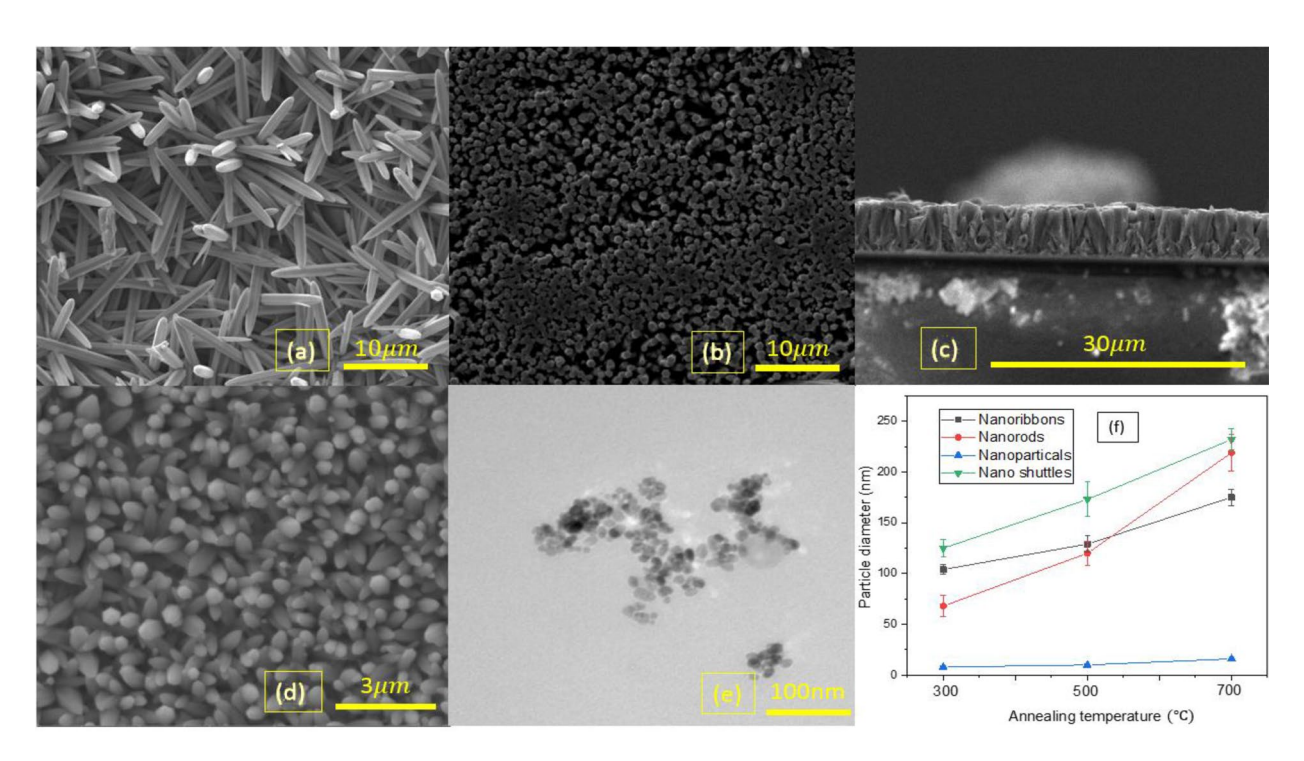


**Figure 1:** SEM images of (a) nanoribbons, (b) nanorods, (c) cross-sectional view of nanorods, (d) nanoshuttles, (e) TEM image of nanoparticles, and (f) nanostructure diameter of nanoribbons, nanorods, nanoparticle, and nanoshuttle.



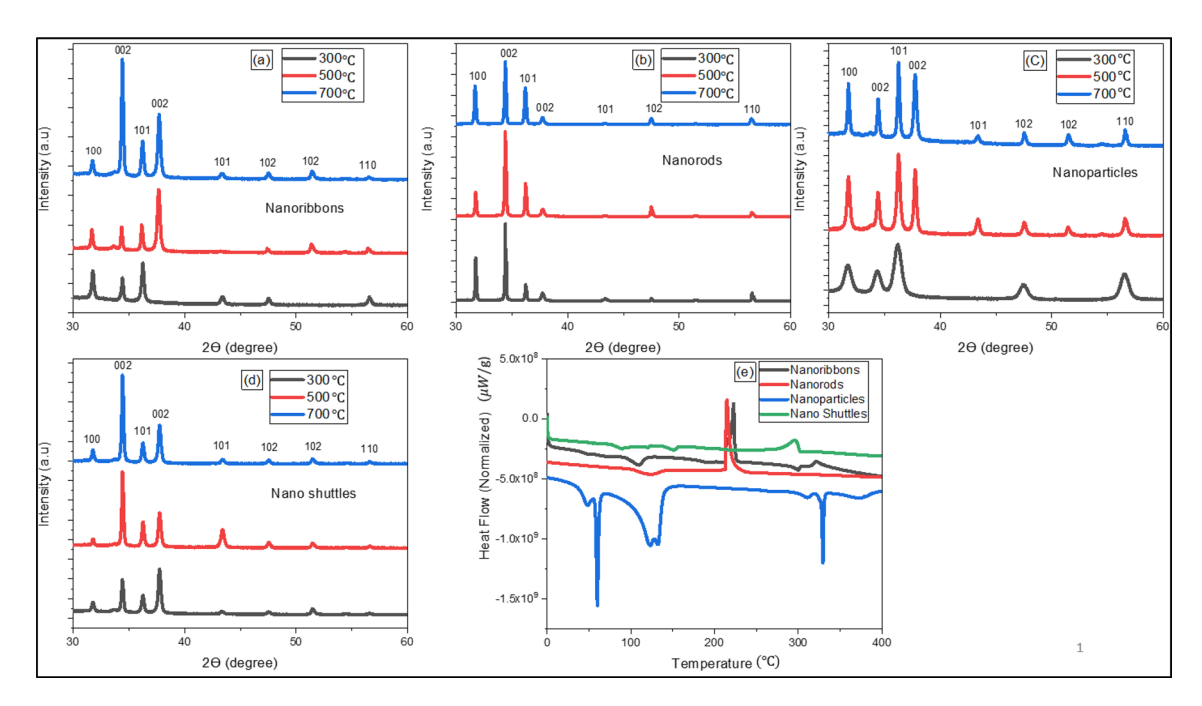


Figure 2: XRD spectra of (a) nanoribbons, (b) nanorods, (c) nanoparticles, (d) nanoshuttles, and (e) DSC analysis of ZnO nanostructures.

also varied the growth of the nanorods along the c-axis [36]. Cho et al. also observed that a better crystallinity in ZnO nanostructures resulted in increasing temperature [37]. This higher crystalline nature may be due to the increased grain size at higher annealing temperatures.

The crystallinity of ZnO nanostructures which are annealed to 300 °C was determined by using Differential Scanning Calorimetry (DSC) from 0 to 400 °C at a rate of 5°C min<sup>-1</sup> in nitrogen atmosphere. Figure 2e shows a comparison of DSC spectra of all ZnO morphologies, namely, nanoribbons, nanorods, nanoparticles, and nanoshuttles. As observed in the DSC plot of nanoparticles, it has three endothermic peaks. The three peaks at 59.94 °C, 132.60 °C, and 329.52 °C may be attributed to the loss of volatile surface molecules absorbed, evaporation of the solvent, and formation of zinc oxide nanoparticles, respectively [38]. All other DSC curves of ZnO nanoribbons, nanorods, and nanoshuttles reveal several endothermic peaks at lower temperatures range (80 °C to 200 °C) and one exothermic peak around temperature range of (200 °C to 300 °C). The lower temperature peaks may be due to volatile surface molecules absorbed, evaporation of the solvent, and the exothermic peak is mainly due to crystallization of wurtzite ZnO [39].

The degree of crystallinity ( $X_c$ ) values of the nanostructures was determined by using the following equation [40]:

$$X_{\rm c} = \frac{\Delta H_{\rm f}}{\Delta H_{\rm f(100)}} \times 100 \tag{1}$$

where  $\Delta H_{\rm f}$  is the heat of fusion of ZnO nanostructures and  $\Delta H_{\rm f(100)}$  is the heat of fusion of 100% ( $\Delta H_{\rm f(100)} = 230\,{\rm J/g}$ ) [41]. The calculated values of the degree of crystallinity for all nanostructures are listed in Table 1. These results also confirmed the purification of ZnO with different morphologies. We observed that nanorods have the highest crystallinity values (17.02%) and nanoparticles have obtained the lowest value (7.59%).

### **Optical studies**

Optical properties were analyzed by UV–Visible Spectroscopy and Photoluminescence (PL) measurements at room temperature. Figure 3 shows UV–Visible absorption spectra and bandgap energy of nanoribbons, nanorods, nanoparticles, and nanoshuttles with different annealing temperatures. All samples were scanned in the wavelength range between 350 and 700 nm. When increasing annealing temperature from 300 to 700 °C, the absorption peaks show a redshift. This redshift can be explained by the effective mass model [42]. With the increasing size of

 TABLE 1: Crystallinity values of different morphologies.

Nano structure name	Peak temperature (°C)	ΔHf	(X <sub>c</sub> )	
Nanoribbons	227.72	38.15	16.59	
Nanorods	214.72	39.14	17.02	
Nanoparticles	329.52	17.45	7.59	
Nano Shuttles	296.52	18.31	7.96	



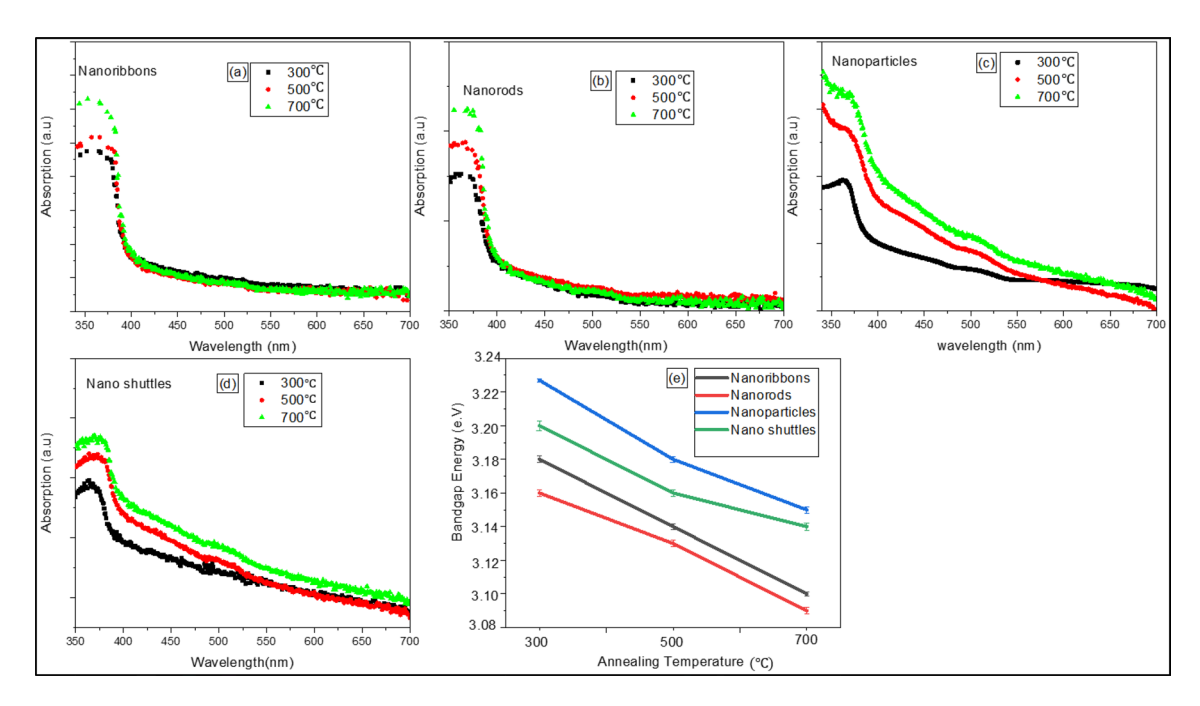


Figure 3: UV-Visible absorption of (a) nanoribbons, (b) nanorods, (c) nanoparticles, (d) nanoshuttles, and (e) variation of bandgap energy with different annealing temperatures.

ZnO nanoparticles, there is also an increase in absorbance. Similarly, Goh et al., have previously reported that the absorbance increases with the increasing size of particles [43]. Alias et al., also showed that the UV-visible absorption strongly depends on the particle size of ZnO [44]. Besides, Raji et al. have reported the UV-Visible absorption over the visible region can be tuned by changing annealing temperature [45]. The absorption data were applied to calculate corresponding bandgap energy using the Tauc plot equation [46].

$$(\alpha h \nu)^2 = A \left( h \nu - E_g \right), \tag{2}$$

where A is the constant for direct transition,  $E_{\rm g}$  is the energy gap, h is Plank's constant, and v is the frequency of incident radiation. The bandgap of all samples was found to decrease with increasing annealing temperature. Among all morphologies, nanorods have shown the lowest bandgap energy for all annealing temperatures. The optical band gap energy of nanorods decreased from 3.16 to 3.09 eV as the annealing temperature increased from 300 to 700 °C. The bandgap energy for nanoparticles was 3.23 eV, 3.19 eV, and 3.17 eV at 300 °C, 500 °C, and 700 °C, respectively.

Photoluminescence (PL) measurements of different ZnO nanostructures are shown in Fig. 4. All PL measurements were performed at room temperature. It can be seen from these figures that all PL spectra consist of three prominent peaks at all annealing temperatures. The lower peak in the UV region corresponds to the near band edge emission (NBE) due to the free excitonic emission of ZnO [47]. The other two peaks in the visible region are attributed to defects such as Zinc interstitials and Oxygen vacancies [48]. All samples show that the

near band edge emission (NBE) peak position shifts to a longer wavelength region with increasing annealing temperature from  $300 \text{ to } 700 \text{ }^{\circ}\text{C}$ .

PL measurements also indicate that the green band emission strongly depends on the morphology of nanostructures and annealing temperatures. From Fig. 4, it is evident that the intensity of the green band increases from 300 to 700 °C. This enhancement may be attributed to the increase in surface defects. Adeel et al. have mentioned that the defects can be enhanced by the visible light absorption ability of ZnO as a result of narrowing the bandgap [49].

Further, the highest green band emission was shown by nanoparticles at 700 °C. The main reason could be the highest surface/volume ratio in nanoparticles compared with other nanostructures. Based on this, nanoparticles could be associated with a high density of surface oxygen vacancies.

# **Electrical resistivity measurements**

Figure 5a and b show the variation in electrical resistivity of four nanostructured ZnO morphologies with annealing temperature. Van der Pauw method was employed to measure the electrical resistivity of nanostructures. In this study, we observe that nanorods have lowest resistivity compared to other nanostructures due to higher aspect ratio. From Fig. 5a, we also observed that as the annealing temperature increased from 300 to 700 °C, ZnO nanorods show continuous decrease in resistivity from 12.86 to 3.59  $\Omega$  cm, respectively. From Fig. 5b, the highest resistivity of 750  $\Omega$  cm was measured in nanoshuttle at



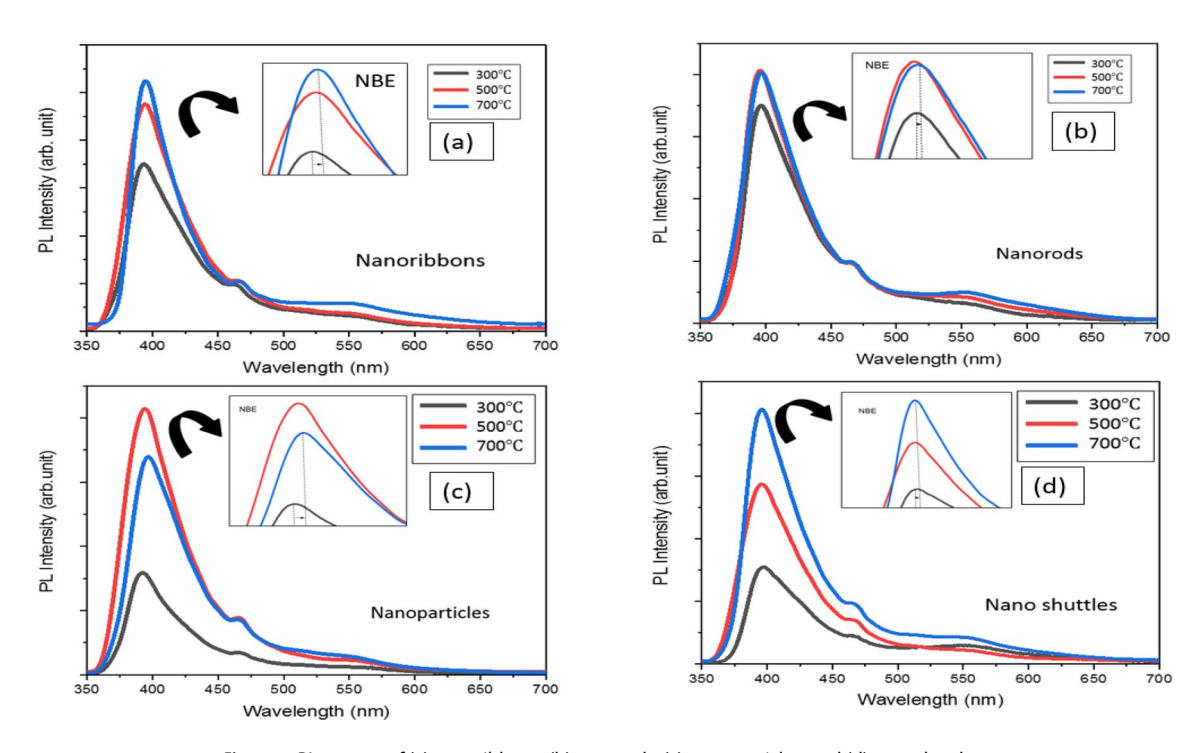


Figure 4: PL spectra of (a) nanoribbons, (b) nanorods, (c) nanoparticles, and (d) nanoshuttles.

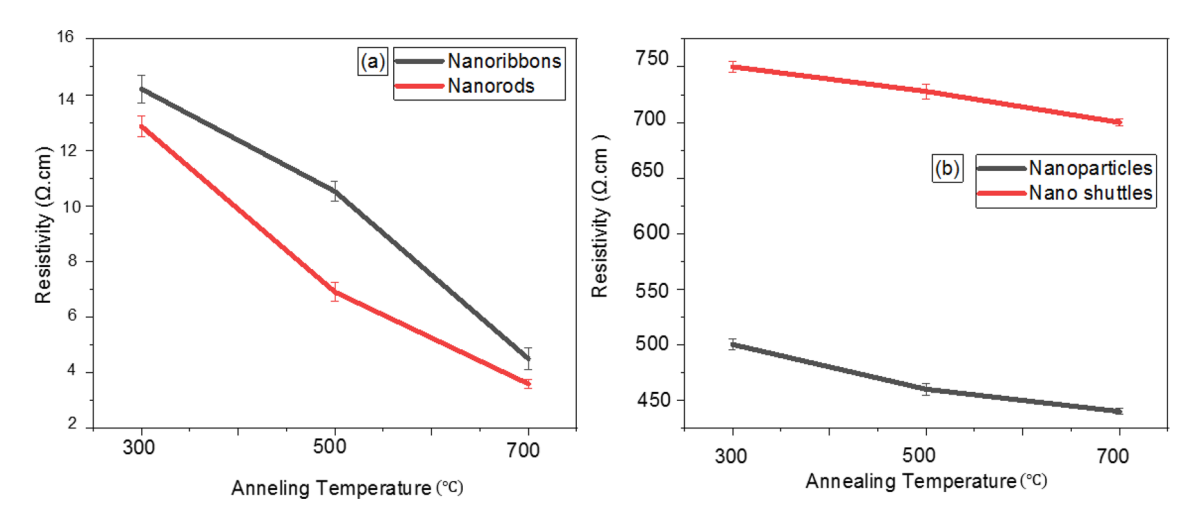


Figure 5: Resistivity of ZnO nanostructures (a), nanoribbons, and nanorods, and (b) nanoparticles and nanoshuttle.

300 °C. In all samples, resistivity data show that resistivity of nanostructures is inversely proportional to the annealing temperature. This decrease in resistivity may be attributed to the expansion of grain size and grain boundaries with increasing annealing temperature. Ganga et al. have previously reported that increasing particle size resulted in a decrease in resistivity because of reducing carrier trapping phenomena [50]. Joseph et al. have noted that high resistivity in nanostructures may be due to the grain boundary effects and semiconductor nature of the ZnO, which creates a potential barrier for transport of

electrons [51]. From electrical resistivity measurements, we observed that the resistivity of ZnO nanostructures depends on several key parameters such as morphology, particle size, and annealing temperature.

### Impedance analysis

Figure 6a, b, c, and d shows the Cole–Cole plot of impedance spectra of four different ZnO nanostructures which are nanoribbons, nanorods, nanoparticles, and nanoshuttles. Electrical transport properties such as grain and grain boundary effects of

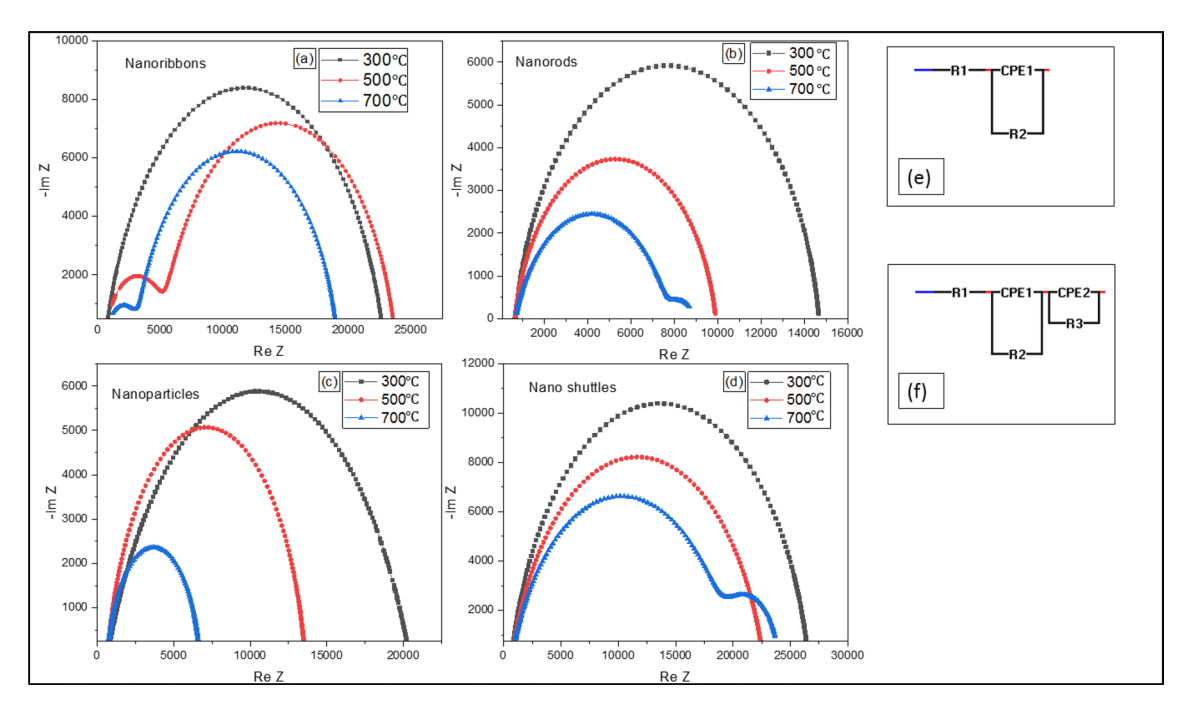


Figure 6: Impedance spectra of ZnO nanostructures (a) nanoribbons, (b) nanorods, (c) nanoparticles, (d) nanoshuttle, and equivalent circuit models (e) of R1-series resistance, R2-grain, grain boundary resistance, and CPE1-constant phase element for grain and grain boundary, (f) R1- series resistance, R2-grain resistance, R3-grain boundary resistance, CPE1-constant phase element for grain, and CPE2-constant phase element for grain boundary.

nanostructures were analyzed by impedance spectroscopy using two equivalent circuit models shown in Fig. 6e and f. In the equivalent circuit, the resistance R1 represents the series resistance which is related to the external circuit elements [52]. The resistance R2 and R3 indicate the interfacial electron transfer resistance, which corresponds to the grain and grain boundary resistance, respectively [53]. Also, CPE1 and CPE2 are the constant phase elements that account for the deviation of the capacitance with grain and grain boundaries. The Cole–Cole plot analysis was done in the frequency range of 100 Hz to 40 MHz. The

fitted parameters, carrier lifetime, and RC time constant of ZnO nanostructures at different annealing temperatures were based on the equivalent circuit models listed in Table 2. The carrier lifetime  $\tau$  (Cole–Cole) was obtained from the reciprocal peak frequency of the large semicircle in the Cole–Cole plot [54].  $\tau$ 1 and  $\tau$ 2 represent the RC time constant ( $\tau$  = RC) of grain and grain boundary, respectively.

The Cole-Cloe plot in the high-frequency region response corresponds to the grain size and a lower frequency response arises from the grain boundaries. We observed that

TABLE 2: Grain and grain boundary parameters of nanostructures extracted from impedance analysis.

Nano structure name	Annealing tem- perature (°C)	<i>R</i> 1 (kΩ)	R2 (kΩ)	R3 (kΩ)	CPE1 (nF)	CPE2 (nF)	τ (Cole–Cole) (μs)	τ1 (μs)	τ2 (μs)
	perature ( C)	N I (K\$2)	NZ (K\$2)	NO (K22)	CFLI (III )	CFLZ (III )	t (Cole-Cole) (μs)	ιι (μ3)	ι 2 (μ3)
Nanoribbons	300	0.68	22.09	-	2.27	-	50.48	6.30	-
	500	0.68	4.59	18.84	2.50	0.05	50.40	0.02	306.56
	700	0.68	2.50	15.92	0.32	2.69	47.30	0.13	6.64
Nanorods	300	0.68	13.99	-	2.04	-	116.76	8.29	-
	500	0.65	9.27	-	5.74	-	69.00	11.21	-
	700	0.68	7.00	2.50	2.38	3.53	31.00	0.64	0.28
Nanoparticles	300	0.69	19.67	-	9.45	-	15.81	3.65	-
	500	0.68	12.87	-	7.21	-	10.20	17.80	-
	700	0.68	5.98	-	4.01	-	23.20	3.74	-
Nano shuttle	300	0.68	25.90	-	1.37	-	69.00	6.79	-
	500	0.69	21.9	-	2.39	-	39.00	5.88	-
	700	0.68	18.94	4.29	3.23	9.65	17.98	3.47	27.00

in all nanostructures, the real part of impedance (resistance) significantly decreased with increasing annealing temperature from 300 to 700 °C. Joshi et al. have reported that the resistivity of polycrystalline material increases with decreasing grain size [55]. This decrease in resistance may be attributed to enhancement in surface and grain boundary area with annealing temperature. At low temperatures, all samples indicated an unresolved semicircle feature due to grain and grain boundaries. From Fig. 6a, b, and d, we noted that nanoribbons, nanorods, and nanoshuttles showed well-defined semicircles due to grain and grain boundaries at a higher temperature. Figure 6a shows that the lowest grain resistance value of  $2.50 \text{ k}\Omega$  was observed from nanoribbons compared to other morphologies at 700 °C annealing temperature. At 300 °C annealing temperature, the lowest unresolved impedance 13.99 k $\Omega$  was obtained from nanorods compared to other nanostructures. When the temperature was varied from 300 to 700 °C, nanorods showed a peak in impedance at 7.00 k $\Omega$ and grain boundary impedance at 2.50 kΩ with 31.00 µs carrier lifetime.

At 300 °C and 500 °C, nanorods showed the highest carrier lifetime as 116.76  $\mu$ s and 69.00  $\mu$ s, respectively, compared to other nanostructures. However, analysis of nanoribbons resulted in the highest carrier lifetime 47.30  $\mu$ s at 700 °C compared to other morphologies. Jin et al. have reported that the longer carrier lifetime of the device has less charge recombination [54]. Therefore, the longer carrier lifetime of devices is more suitable for photovoltaic applications. From our analysis of impedance measurements on various ZnO morphologies, it can be observed that impedance spectra parameters crucially depend on the size of nanostructures, morphology, and annealing temperatures.

#### **Contact angle measurements**

Contact angle (CA) measurements of four different ZnO nanostructures are shown in Fig. 7. The Sessile drop method was employed to measure the contact angle. If CA is less than 90° then the surface is called a hydrophilic surface and if CA is more than 90° but less than 150° then it is known as a hydrophobic surface. The surface is called superhydrophobic when CA is above 150°. To get a hydrophobic or superhydrophobic contact angle, all ZnO substrates were modified with a monolayer of 1H,1H,2H,2H perfluorodecyltriethoxysilane. Wetting properties were studied with CA measurements with water and ethylene glycol as test liquids. From CA measurements, we obtained that surface with ZnO nanoparticles has hydrophobic properties while nanorods, nanoribbons, and nanoshuttles resulted in a superhydrophobic surface. Surface Free Energy of ZnO substrates was determined based on contact angle data by the Owens-Wendt (Extended Fowkes) Model [56]. Using the equation:

$$\frac{\gamma_1(\cos \theta + 1)}{2(\gamma_1^d)^{1/2}} = (\gamma_s^p)^{1/2} \frac{(\gamma_1^p)^{1/2}}{(\gamma_1^d)^{1/2}} + (\gamma_s^d)^{1/2}$$
(3)

where  $\gamma_1$  is the liquid free surface energy,  $\gamma_1^d$  and  $\gamma_1^p$  are the liquid dispersive and polar components, respectively,  $\gamma_s$  is the solid free surface energy,  $\gamma_s^d$  and  $\gamma_s^p$  are the solid dispersive and polar components, respectively. Surface energy components of test liquids, which are water ( $\gamma_1^p = 51 \text{ mJ/m}^2$ ,  $\gamma_1^d = 21.8 \text{ mJ/m}^2$ ,  $\gamma_1 = 72.8 \text{ mJ/m}^2$ ) and ethylene glycol ( $\gamma_1^p = 19 \text{ mJ/m}^2$ ,  $\gamma_1^d = 29.0 \text{ mJ/m}^2$ ,  $\gamma_1 = 48.0 \text{ mJ/m}^2$ ) [57].

Table 3 summarizes the values of the surface free energy  $(\gamma_s)$ , the dispersive parts  $(\gamma_s^d)$ , and the polar parts  $(\gamma_s^p)$  for ZnO nanostructures. Figure 7 indicates that CA measurements on ZnOnanostructured film substrates prepared by all morphologies

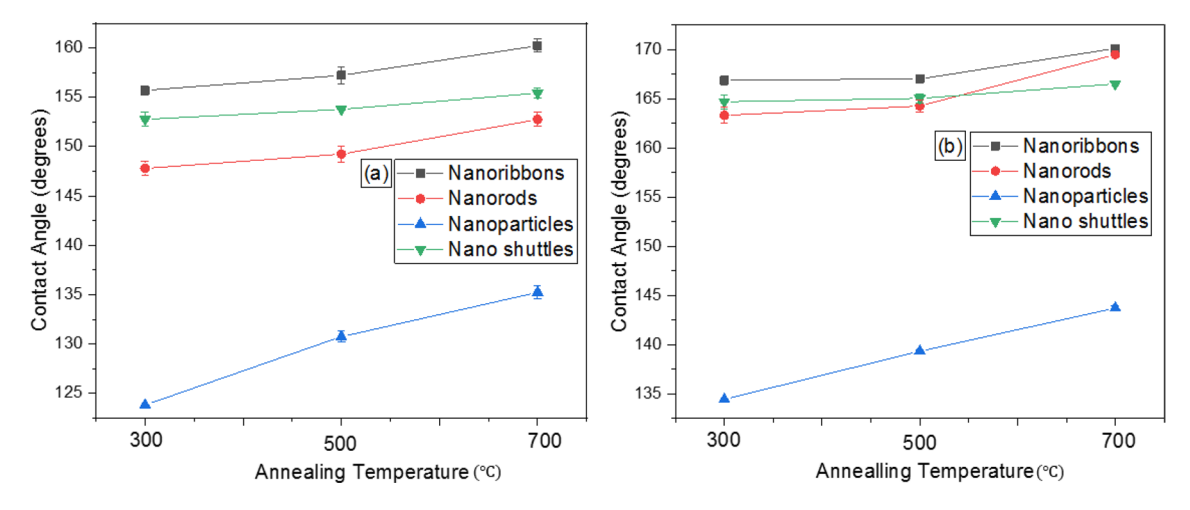


Figure 7: Contact angle of ZnO nanostructures of nanoribbons, nanorods, nanoparticles, and nanoshuttle with (a) ethylene glycol and (b) water droplet.



TABLE 3: Surface energies of ZnO nanostructures.

Nano structure name	Annealing tem- perature (°C)	$\gamma_s^p  (\text{mJ/m}^2)$	$\gamma_{\rm s}^{\rm d}$ (mJ/m <sup>2</sup> )	$\gamma_{\rm s}$ (mJ/m <sup>2</sup> )
Nanoribbons	300	0.0711	0.3730	0.4442
	500	0.0423	0.2640	0.3064
	700	0.0417	0.1832	0.2249
Nanorods	300	0.2463	1.1815	1.4278
	500	0.2132	1.0006	1.2138
	700	0.2557	0.8172	1.0729
Nanoparticles	300	0.2518	2.4647	2.7165
	500	0.2156	1.3727	1.5883
	700	0.0921	1.0965	1.1886
Nano Shuttles	300	0.0911	0.5445	0.6356
	500	0.0731	0.4590	0.5321
	700	0.0687	0.3795	0.4482

showed an increase from 300 to 700 °C for both water and ethylene glycol. At 300 °C, the highest CA (166.9°) was obtained by nanoribbons and the lowest CA (134.4°) was shown by nanoparticles. A similar trend was also obtained at higher annealing temperatures, the nanoribbons have the highest CA (170.1°), and the nanoparticles have the lowest CA value as (143.72°) at 700 °C. Wang et al. reported that CA value can be dependent on the micro/ nanoscale hierarchical structure and chemical modification [58]. From our experimental observations, it can be concluded that CA is directly proportional to the size of nanostructures and annealing temperatures. Similarly, Munshi et al. observed a decrease in CA with a decrease in the size of nanoparticles [59]. Also, a theoretical analysis by Munshi et al. showed that CA strongly depends on the size of nanoparticles. As a result, the surface free energy increases with decreasing particle size, because of the large surface area in small nanoparticles. Surface free energy may be the strong reason for changing CA with morphology and particle size.

The surface free energy of ZnO substrates decreased from 300 to 700 °C for all morphologies. The lowest surface free energy was obtained by nanoribbons compared with other morphologies at all annealing temperatures. Nanoribbon's surface free energy value decreased from 0.4442 to 0.2249 mJ/m² as the annealing temperature increased from 300 to 700 °C, respectively. From these Wettability studies, we observed that the surface free energy of ZnO-nanostructured substrates depend on morphology, annealing temperature, and the size of nanostructures.

## **Discussion**

In our study, we have verified that various ZnO nanostructures can be obtained by changing pH values, chemical compositions, and synthesis methods. We observed that the morphology and particle size can influence optical, electrical, and surface properties of ZnO

nanostructures. With increasing annealing temperature, all nanostructures increase in size as observed from SEM and TEM measurements. For all morphologies, UV-Visible absorbance increased with increasing annealing temperature and shifted to a longer wavelength region. This enhancement in absorption with annealing temperatures in all nanostructures can be attributed to the increase in grain size and improvements in crystallinity with heat treatments. Our results indicate that the grain size and crystallinity improved with annealing temperature which was also verified by XRD analysis (Fig. 2). DSC results confirmed the purify of all ZnO nanostructures (Fig. 2e). Redshift with an increase in nanostructure size was confirmed by PL measurements. UV-Visible measurements also show that the absorbance strongly depends on the morphology of nanostructures. Measurements of bandgap energy exhibit variations with morphology and the bandgap decrease with increasing particle size. As we anneal, the grain boundaries expand in random directions. This expansion results in a reduction in surface energy and is consistent with the reduction in X-ray intensity along the c-axis in various morphologies (Fig. 2). Enhancement in grain boundaries and grain size with annealing temperature is also reflected in the reduction in resistivity with annealing temperature. With increasing annealing temperature, the defect density in ZnO will be enhanced. This effect can be observed from the increasing intensity peak of green emission in PL spectra (Fig. 4). At higher annealing temperatures, we observed enhancement in grain size and crystallinity as revealed by XRD studies (Fig. 2). As a result, annealing of samples reduced the charge carrier scattering at grain boundaries and improved the mobility as revealed by resistivity measurements (Fig. 5). Impedance analysis (Fig. 6) also confirmed that the transport properties change with the morphology and size of nanostructures. We can correlate the important role of grain and grain boundaries at higher temperatures from impedance studies. Impedance analysis at various annealing temperatures (Fig. 6) indicate that grains and grain boundary are very crucial in mediating transport properties of ZnO morphologies. Impedance analysis shows that the ZnO morphology with a higher carrier lifetime is the most suitable for photovoltaic applications because the charge recombination process is reduced in this material. Our results support that there are changes in the contact angle due to morphology and size variation of ZnO nanostructures. We observed that the contact angle increases with the size of nanostructures, which may be due to the enhancement of the surface roughness and reduction of surface free energy of ZnO structures with morphological changes.

## **Conclusions**

We have synthesized ZnO with different nanostructures, namely, nanoribbons, nanorods, nanoparticles, and nanoshuttles, and investigated the structural, electrical, and optical properties at three different annealing temperatures (300 °C,



500 °C, and 700 °C). Morphology and structural properties of nanostructures were studied using SEM, TEM, DSC, and XRD methods. Optical properties were analyzed using UV-Visible and PL techniques. Bandgap in all samples was found to decrease with increasing annealing temperature. Electrical measurements indicated that the resistivity of samples depends on morphology and annealing temperature. The lowest resistivity of 3.59 Ωcm was obtained from nanorods at 700 °C, while the highest resistivity of 750 Ωcm was obtained by nanoshuttle at 300 °C. The transport properties of nanostructures were investigated using impedance analysis. At low temperatures, all samples indicated an overlapped semicircle feature due to grain and grain boundaries. Therefore, grain boundary analysis is not possible for low annealing temperature for ZnO morphologies. Nanoribbons, nanorods, and nanoshuttles showed well-defined semicircles due to grain and grain boundaries at the higher temperature. The lowest grain boundary impedance of 2.50 kΩ of nanorods was compared with impedance of other nanostructures at 700 °C. The nanoribbons showed the lowest grain resistance at 2.50 k $\Omega$  at 700 °C. We also observed that the grain and grain boundary resistance decreased with increasing temperature in all samples. From the analysis of Impedance spectra, we observe that electrical resistance depends on the size and morphology of nanostructures. The wetting behavior of the surfaces increases with nanostructure size, which can be specially controlled by annealing temperature and morphology of nanostructures. Overall, ZnO nanorods and nanoribbons have shown the optimum transport properties from the impedance analysis. Hence, ZnO nanoribbons and nanorods may be used for developing electrodes for nanostructured ZnO-based dyesensitized solar cells and other devices.

#### **Materials and methods**

#### Materials

Zinc acetate dehydrate (Zn (CH<sub>3</sub>COO)<sub>2</sub> .2H<sub>2</sub>O, > 99.5%), Zinc nitrate hexahydrate (Zn (NO<sub>3</sub>)<sub>2</sub> .6H<sub>2</sub>O, > 99.5%), Hexamethylenetetramine (C<sub>6</sub>H<sub>12</sub>N<sub>4</sub>, > 98%), Sodium hydroxide (NaOH, > 97%), Ammonium hydroxide (NH<sub>4</sub>OH, 28-30%), Ethyl alcohol (C<sub>2</sub>H<sub>6</sub>O, > 98%), Acetic acid (CH<sub>3</sub>CO<sub>2</sub>H,  $\geq$  99%), and Triton X-100 (t-Oct-C<sub>6</sub>H<sub>4</sub>-(OCH<sub>2</sub>CH<sub>2</sub>)<sub>x</sub>OH, x=9–10) were purchased from Sigma Aldrich (USA).

## Seed layer deposition

ZnO seed layer was deposited on Fluorine-doped tin oxide (FTO) by using the sputtering technique with zinc target. Then the FTO substrate was annealed for 1 h to deposit the seed layer.

## Preparing ZnO nanoribbons

ZnO nanoribbons were prepared by the chemical bath deposition (CBD) method. Firstly, Zinc nitrate hexahydrate (0.1 M) was dissolved in water and stirred for 1 h. While continuing stirring ammonium hydroxide was added to the solution until it reached the pH of the reaction mixture at 9. Then seeded substrate was vertically suspended in the resultant solution in a convection oven at 95 °C for 5 h. Finally, the samples were annealed in a furnace at 300 °C, 500 °C, and 700 °C for 1 h in the air.

## **Preparing ZnO nanorods**

ZnO nanorods were synthesized using a chemical bath deposition (CBD) method. Firstly, an equimolar (0.1 M) solution of Zinc nitrate hexahydrate and hexamethylenetetramine were mixed for 2 h. Then, a seeded substrate was vertically kept in the resultant solution (PH 7) for 6 h at 95 °C in an oven. After that, samples were separately annealed in a furnace at three different temperatures, 300 °C, 500 °C, and 700 °C in air.

## **Preparing ZnO nanoparticles**

Firstly, Zinc acetate dehydrates (0.1 M) were dissolved in ethanol and thoroughly mixed using a magnetic stirrer for 30 min. Then Sodium hydroxide was added dropwise to Zine acetate solution until it reached the pH of the reaction mixture at 10. After that resultant solution was transferred into a commercial microwave (Model No. EM720CGA-PMB) for 2 min at a 210 W power level. The final solution was centrifuged and washed with distilled water several times. The precipitated ZnO nanoparticles were dried at 300 °C for 1 h. After that, prepared ZnO nanoparticles were grounded with Triton X-100, acetic acid, and ethanol. A thin film of the resultant mixture was deposited on Fluorine-doped tin oxide (FTO) glass sides using the doctor blade method. Finally, samples were annealed in a furnace at 300 °C, 500 °C, and 700 °C in air.

## Preparing ZnO nanoshuttle

Zinc nitrate hexahydrate (0.1 M) was dissolved in water and stirred for 1 h. Ammonium hydroxide was added dropwise to make the pH of the reaction mixture at 9. Then a seeded substrate was suspended in solution and was transferred into a commercial microwave (Model No. EM720CGA-PMB) for 15 min at 210 W power level. Finally, samples were heated in a furnace at different annealing temperatures, 300 °C, 500 °C, and 700 °C, in air.

The prepared different ZnO nanostructures were characterized by scanning electron microscopy (SEM), transmission electron microscopy (TEM), X-ray diffraction (XRD), differential



Scanning Calorimetry (DSC), UV–Visible absorption techniques, Photoluminescence (PL), resistivity measurements, impedance Spectroscopy, and contact angle measurements.

# **Acknowledgments**

The authors are thankful to Rick Portman for helping with TEM and SEM measurements, Dr. Alexie Grigoriev for assisting XRD measurement, and Dr. Gabriel LeBlanc for DSC measurements.

## **Author contributions**

The manuscript was written through the contributions of all authors. All authors have approved the final version of the manuscript.

# **Funding**

This research was funded by NASA EPSCoR, Grant Number 14-2-1205324.

# **Data availability**

The datasets generated during this study are available from the corresponding author on reasonable request.

### **Declarations**

Conflicts of interest The authors declare no conflict of interest.

# References

- D.P. Norton, Y.W. Heo, M.P. Ivill, K. Ip, S.J. Pearton, M.F. Chisholm, T. Steiner, Mater. Today 7, 34 (2004)
- 2. M. Thirumavalavan, K.L. Huang, J.F. Lee, Materials **6**, 4198 (2013)
- S. Talam, S.R. Karumuri, N. Gunnam, ISRN Nanotechnol., 1 (2012)
- 4. K.P. Trilok, K. Vinod, H.C. Swart, L.P. Purohit, Physica E 77, 1
- A. Blakers, N. Zin, K.R. Mcintosh, K. Fong, Energy Procedia 33, 1 (2013)
- E. Topoglidis, A.E.G. Cass, B. O'Regan, J.R. Durrant, J. Electroanal. Chem. 571, 20 (2001)
- X.L. Cheng, H. Zhao, L.H. Huo, S. Gao, J.G. Zhao, Sensor Actuator B 102, 248 (2004)
- Y. Hames, Z. Alpaslan, A. Kösemen, S.E. San, Y. Yerli, Sol. Energy 84, 426 (2010)
- P.V. Adhyapak, S.P. Meshram, I.S. Mulla, S.K. Pardeshi, D.P. Amalnerkar, Mater. Sci. Semicond. Process. 27, 197 (2014)

- K. Keis, C. Bauer, G. Boschloo, A. Hagfeldt, K. Westermark,
   H. Rensmo, H. Siegbahn, J. Photochem. Photobiol., A 148, 57 (2002)
- L. Luo, Y. Zhang, S.S. Mao, L. Lin, Sensor Actuator A 127, 201 (2006)
- 12. P. Bindu, S. Thomas, J. Theor. Appl. Phys. 8, 123 (2014)
- 13. N. Singh, P. Pandey, F.Z. Haque, Optik 123, 1340 (2012)
- C. Gu, J. Huang, Y. Wu, M. Zhai, Y. Sun, J. Liu, J. Alloys Compd. 509, 4499 (2011)
- F. Yang, W.H. Liu, X.W. Wang, J. Zheng, R.Y. Shi, H. Zhao, H.Q. Yang, A.C.S. Appl, Mater. Interfaces 4, 3852 (2012)
- O.W. Kennedy, M.L. Coke, E.R. White, M.S.P. Shaffer, P.A. Warburton, Mater. Lett. 212, 51 (2018)
- 17. J. Ding, X. Fang, R. Yang, B. Kan, X. Li, N. Yuan, Nanoscale Res. Lett. **9**, 1 (2014)
- M.I. Qadir, S.J. Rana, O. Nur, M. Willander, J. Lu, L. Hultman, J. Mater. Res. 29, 2425 (2014)
- G.R. Neupane, A. Kaphle, P. Hari, Sol. Energy Mater. Sol. C 201, (2019)
- M. Arif, M. Shakir, S. Nfaify, V. Ganesh, A. Sanger, H. Algarni,
   P.M. Vilarinno, A. Singh, J. Mater. Res. 34, 1309 (2019)
- M. Kawakami, A.B. Hartanto, Y. Nakata, T. Okada, Jpn. J. Appl. Phys. 42, L33 (2003)
- H. Wang, J. Xie, K. Yan, M. Duan, J. Mater. Sci. Technol. 27, 153 (2011)
- 23. M.T. Htay, Y. Hashimoto, K. Ito, Jpn. J. Appl. Phys. 46, 440 (2007)
- J. Huang, C. Xia, L. Cao, X. Zeng, X. Mater, Sci. Eng. B 150, 187 (2008)
- 25. L.J. An, J. Wang, T.F. Zhang, H.L. Yang, Z.H. Sun, Adv. Mater. Res. **380**, 335 (2011)
- 26. A. Kaphla, P. Hari, Appl. Phys. 122(16), (2017)
- F. Huber, A. Puchinger, W. Ahmad, M. Madel, S. Bauer, K. Thonke, J. Mater. Res. 32, 4087 (2017)
- R. Wahab, S.G. Ansari, Y.S. Kim, M. Song, H.S. Shin, Appl. Surf. Sci. 255, 4891 (2009)
- H. Zhang, D. Yang, X. Ma, Y. Ji, J. Xu, D. Que, Nanotechnology 15, 622 (2004)
- T. Andelman, Y. Gong, M. Polking, M. Yin, I. Kuskovsky, G. Neumark, S. O'Brien, J. Phys. Chem. B 109, 14314 (2005)
- 31. W. Zhang, X. Chen, N. Xu, R. Xiang, Y. Zhu, Z. Tang, J. Nanomater., 986157 (2013)
- 32. W.J. Li, E.W. Shi, T. Fukuda, Cryst. Res. Technol. 38, 847 (2003)
- 33. O.A. Yildirim, C. Durucan, J. Mater. Res. 27, 1452 (2012)
- E.A. Batista, A.C.A. Silva, T.K.D.L. Rezende, E.V. Guimaraes,
   P.A.G. Pereira, P.E.N.D. Souza, R.S.D. Silva, P.C.D. Morais, N.O.
   Dantas, J. Mater. Res. 36, 1 (2021)
- R. López, T. Díaz, G. García, E. Rosendo, R. Galeazzi, A. Coyopol, H. Juárez, M. Pacio, F. Morales, A.I. Oliva, Adv. Mater. Sci. Eng., 257494 (2014)



- D. Badawy, S. Soltanian, P. Servati, A. Bahi, F. Ko, J. Mater. Res. 35, 3091 (2020)
- 37. S. Cho, Trans. Electr. Electron. Mater. 10, 185 (2009)
- 38. N. Mayedwa, A.T. Khalil, N. Mongwaketsi, N. Matinise, Z.K. Shinwari, M. Maaza, Nano. Res. Appl. 3, 2 (2017)
- S.B. Majumder, M. Jain, P.S. Dobal, R.S. Katiyar, Mater. Sci. Eng. B103, 16 (2003)
- 40. O.W. Guirguis, M.T.H. Moselhey, Nat. Sci. 4, 57 (2012)
- 41. D.R. Lide, CRC Handbook of Chemistry & Physics, 79th edn. (CRC Press, Boca Raton, 1998)
- 42. N.E. Makori, A.O. Duke, O.M. Cliff, Chem. Res. J. 2(5), 15 (2017)
- 43. E.G. Goh, X. Xu, P.G. McCormick, Scr. Mater. 78–79, 49 (2014)
- S.S. Alias, A.B. Ismail, A.A. Mohamad, J. Alloys Compd. 499, 231 (2010)
- 45. R. Raji, K.G. Gopchandran, J. Sci.: Adv. Mater. Devices 2, 51 (2017)
- 46. M. Caglar, S. Iligan, Y. Caglar, Thin Solid Films 517, 5023 (2009)
- D.M. Bagnall, Y.F. Chen, M.Y. Shen, Z. Zhu, T. Goto, T. Yao, J. Cryst. Growth 184–185, 605 (1998)
- 48. S. Bethke, H. Pan, B.W. Wessels, Appl. Phys. Lett. 52, 138 (1988)

- 49. M. Adeel, M. Saeed, I. Khan, M. Muneer, N. Akram, ACS Omega **6**, 1426 (2021)
- 50. G.R. Neupane, P. Hari, ChemistrySelect 5, 11596 (2020)
- 51. B. Joseph, K.G. Gopchandran, P.K. Manoj, P. Koshy, V.K. Vaidyan, Bull. Mater. Sci. 22, 921 (1999)
- 52. J. Song, E. Zheng, L. Liu, X.F. Wang, G. Chen, W. Tian, T. Miyasaka, Chem. Sus. Chem. **9**, 2640 (2016)
- 53. P.K. Kannan, R. Saraswathi, J. Mater. Res. 32, 2800 (2017)
- Z. Jin, M. Yuan, H. Li, H. Yang, Q. Zhou, H. Liu, X. Lan, M. Liu,
   J. Wang, E.H. Sargent, Y. Li, Adv. Funct. Mater. 26(29), 5284
   (2016)
- 55. D.P. Joshi, K. Sen, Sol. Cells 9(4), 261 (1983)
- 56. S.K. Rawal, A.K. Chawla, V. Chawla, R. Jayaganthan, R. Chandra, Thin Solid Films **519**, 7686 (2011)
- N. Selvakumar, H.C. Barshilia, K.S. Rajan, J. Appl. Phys. 108, 013505 (2010)
- Y. Wang, Y. Liu, L. Zhang, M. Zhang, G. He, Z. Sun, Appl. Surf. Sci. 496, 143743 (2019)
- A.M. Munshi, V.N. Singh, M. Kumar, J.P. Singh, J. Appl. Phys. 103, 084315 (2008)